ARTICLE   OPEN

Mo content-depended competition between Cr_2O_3 enrichment and selective dissolution of $CoCrFeNiMo_x$ high entropy alloys

Qian Hu [1], Cheng-Ping Ye[1], Shang-Chen Zhang[1], Xian-Zong Wang [1✉], Cheng-Feng Du [1✉] and Haifeng Wang[1✉]

The corrosion and passivation behavior of the as-cast $CoCrFeNiMo_x$ ($x = 0$, 0.2, 0.4, 0.6, 0.8, and 1.0) high entropy alloys (HEAs) are investigated. With the addition of Mo, increasing Mo and Cr riched σ phase precipitates from the primary FCC phase. The corrosion resistance of the $CoCrFeNiMo_x$ HEAs strongly depends on the phase structure and the passive film. Generally, Mo promotes the selective dissolution of the FCC phase and the enrichment of Cr_2O_3 in the passive film, the former deteriorates the corrosion resistance while the latter enhances it. Interestingly, the hypoeutectic $Mo_{0.6}$ exhibits a higher corrosion resistance than that of $Mo_{0.4}$, eutectic $Mo_{0.8}$, and hypereutectic Mo_1. Analysis of surface passive film and the composition of alloy phases implies that the Cr_2O_3 enrichment dominates in $Mo_{0.6}$ while selective dissolution governs in Mo_x ($x = 0.4$, 0.8, and 1.0). Mo content-depended competition between the Cr_2O_3 enrichment and selective dissolution is discussed.

INTRODUCTION

High entropy alloys (HEAs), which consist of multiple principal elements in equimolar or near-equimolar ratios have attracted extensive attention due to their breakthrough in the traditional alloy design concept and the performance particularity caused by the multi-principal disordered solid solution phase structure[1,2]. In recent years, various HEAs that exhibit good hardness, high wear resistance, and good structural stability at high temperatures have developed[3–5]. Among them, the CoCrFeNi alloy with a face-centered cubic (FCC) structure has received wide interest due to its good ductility and fracture toughness[6]. In addition to the mechanical properties, most HEAs generally have good corrosion resistance due to their easy formation of a single solid solution structure and contain various passivation alloy elements, such as Cr, Ti, and Mo, and have high application potential in the field of anti-corrosion engineering[7].

Recently, the corrosion behavior of some kinds of CoCrFeNi-based HEAs alloy in aqueous solution has been reported. Ye et al.[8] reported CrMnFeCoNi coating has better corrosion resistance than A36 steel substrate in H_2SO_4 solution due to its obvious passivation behavior. However, Luo et al.[9] investigated the low content of Cr and the extensive formation of metal hydroxide in the passive film are responsible for the lower corrosion resistance of CrMnFeCoNi HEA than 304 L stainless steel in H_2SO_4 solution. In NaCl solution, the corrosion starts from Cr-depleted interdimeric, forming galvanic corrosion with Cr-rich dendrites and making CrMnFeCoNi HEA corrosion resistance degrade[8]. Moreover, Qiu et al.[10] and Wang et al.[11] investigated the corrosion resistance of $Al_2CrFeNiCoCuTi_x$ and $CoCrFeNiTi_x$ HEAs, which showed the beneficial effect of Ti in forming the dense passive film rich in TiO_2 and Cr_2O_3. The influence of Al on the corrosion of HEAs has been widely reported. Kao et al.[12] revealed the corrosion resistance of $Al_xCoCrFeNi$ ($x = 0$, 0.25, 0.50, 1.00) in H_2SO_4 solution. Although the addition of Al increased the thickness of the passive film, Al_2O_3 was easy to form a porous film on the metal surface. And the selective dissolution of Al and Ni has a negative effect on the corrosion resistance of the alloy[12–14]. At the same time, some

studies have shown that the addition of Al has no obvious negative effect on the corrosion resistance of the alloy, such as in $CrFeMoVAl_x$[15] and $FeCoNiCrCu_{0.5}Al_x$[16].

As to the effect of Mo on the corrosion behavior of HEAs, most of them focused on the galvanic corrosion of the alloys and the role of Mo on pitting resistance in NaCl solution. Generally, Mo addition improved the pitting resistance and self-repairing ability of passive film in NaCl solution, which due to the MoO_4^{2-} species could inhibit pitting and promote the formation of Cr oxide-based inner layer[17]. Niu et al.[18] studied the corrosion behavior of the as-annealed $CoCrFeNiMo_x$ HEAs ($x = 0$, 0.2, 0.5, 0.8, 1) in artificial seawater solution, the result showed that the passive film became denser, and the overall dissolution rate decreased by appropriate Mo addition, which could depend on the formation of Mo-oxide film, besides Cr_2O_3 film. However, although Mo-oxides can improve the self-repairing capabilities of the passive film in NaCl solution, the multiple role of Mo in the corrosion resistance of HEAs in acidic solution is rarely reported. For instance, Chou et al.[19] evaluated the corrosion behaviors of $Co_{1.5}CrFeNi_{1.5}Ti_{0.5}Mo_x$ HEAs in 0.5 M H_2SO_4 solution, which were fairly similar. This might be due to the highly acidic environment greatly facilitating the corrosion part, while leaving the passivation part a secondary process. Therefore, in order to further reveal the effect of Mo content on the passivation and dissolution behaviors of CoCrFeNiMo_x HEAs in acidic conditions, more detailed studied on the HEAs in weaker acidic environments are urgently needed.

In the present work, we produced as-cast $CoCrFeNiMo_x$ ($x = 0$, 0.2, 0.4, 0.6, 0.8, and 1.0) HEAs and compared their corrosion behavior in 5 mM H_2SO_4 solution. The microstructure characterizations were investigated by X-ray diffraction (XRD), scanning electron microscope (SEM), and electron backscatter diffraction (EBSD). And the Volta potential maps were acquired by scanning kelvin probe force microscopy (SKPFM). The electrochemical behavior was evaluated by potentiodynamic and potentiostatic polarization, Mott–Schottky, and electrochemical impedance spectroscopy (EIS). In addition, the passive film was analyzed with X-ray photoelectron spectroscopy (XPS) detailed depth profile.

[1]State Key Laboratory of Solidification Processing, Center of Advanced Lubrication and Seal Materials, Northwestern Polytechnical University, Xi'an 710072, PR China.
✉email: xianzong.wang@nwpu.edu.cn; cfdu@nwpu.edu.cn; haifengw81@nwpu.edu.cn

Finally, this paper concentrated on the effect of Mo-induced evolution in alloy structure and passive film composition, and their influences on the corrosion resistance in dilute H_2SO_4 solution. Especially, the competition between passivation and dissolution was further discussed.

RESULTS AND DISCUSSION

### Phase composition and microstructure

Figure 1 shows the XRD patterns of as-cast CoCrFeNiMo$_x$ HEAs. The CoCrFeNi matrix alloy displays FCC single-phase solid solution structure. With the addition of Mo, the diffraction peaks of the FCC phase shift toward the lower 2θ angle, due to the solute atom Mo can induce lattice expansion[18]. Significantly, for the Mo$_0$ and Mo$_{0.4}$ HEAs, there appears obvious [200] texture seen from the abnormal
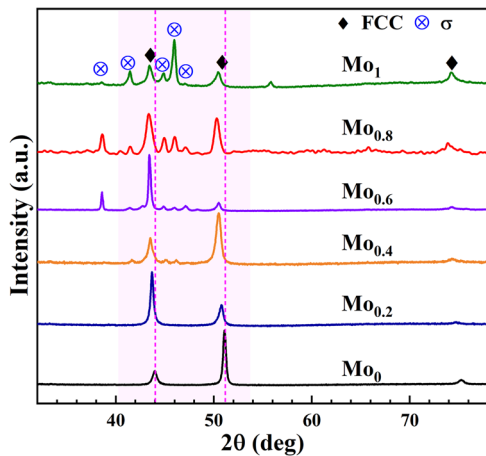

Fig. 1 XRD patterns of the CoCrFeNiMo$_x$ HEAs. XRD results of CoCrFeNiMo$_x$ (x = 0, 0.2, 0.4, 0.6, 0.8, 1) HEAs, including FCC phase and σ-phase.

peak intensity ratios[20]. When the molar ratio of Mo is over 0.4, the precipitated phase gradually appears to mitigate the lattice distortion. The secondary phase is identified as the σ-phase, and its structure is close to a tetragonal FeCrMo phase, according to JCPDS card number 09-0050[21]. The total intensity of the σ-phase is significantly increasing with elevating Mo content. In the Mo$_1$, the σ-phase becomes the main phase structure beyond the FCC phase.

Figure 2 shows the SEM images of CoCrFeNiMo$_x$ (x = 0, 0.2, 0.4, 0.6, 0.8, 1) HEAs. The EBSD phase maps of CoCrFeNiMo$_x$ HEAs are present in Fig. 3, in which the blue and yellow stand for the FCC phase and σ-phase, respectively. CoCrFeNi HEA has a single-phase FCC structure (Figs. 2a and 3a), which is consistent with the XRD results. It can be seen from the SEM image (Fig. 2b) that the Mo$_{0.2}$ has a similar dendrite structure. And according to EDS results (Supplementary Fig. 1), the dendrite structure is rich in Mo, but XRD and EBSD results show both these two phases determined to be the FCC phase. This phenomenon has also been reported in previous literature. Both Shun et al.[21] and Guo et al.[22] investigated that in the CoCrFeNiMo$_{0.2\sim0.3}$, the interdendrite and dendrite are determined to be the FCC phase, and their major difference is the content of Mo. The second phase gradually precipitates as dendrite from the FCC matrix when the molar ratio of Mo increases to 0.4 (Figs. 2c and 3c). The EDS mappings are shown in Supplementary Fig. 1 and the chemical compositions for each phase are summarized in Table 1, in which the σ-phase is rich in Mo and Cr. According to the electronhole theory, as applied to superalloys[18], Cr and Mo are two key elements in the formation of σ-phases, since they both have a larger electron hole number than most transition elements. For Mo$_{0.6}$ (Fig. 2d, g), the microstructure change to typically hypoeutectic: one of which is a bulk-like structure and another is a eutectic-like structure. The hypoeutectic structure also can be inferred from the EBSD results (Fig. 3d), in which the bulk is the FCC phase and the eutectic-like region is the eutectic structure composed of the FCC phase and σ-phase. The fully eutectic layered structure is obtained in Mo$_{0.8}$ (Fig. 3e). And the lamellar spacing of the Mo$_{0.8}$ alloy is about 320 nm (Fig. 2h).
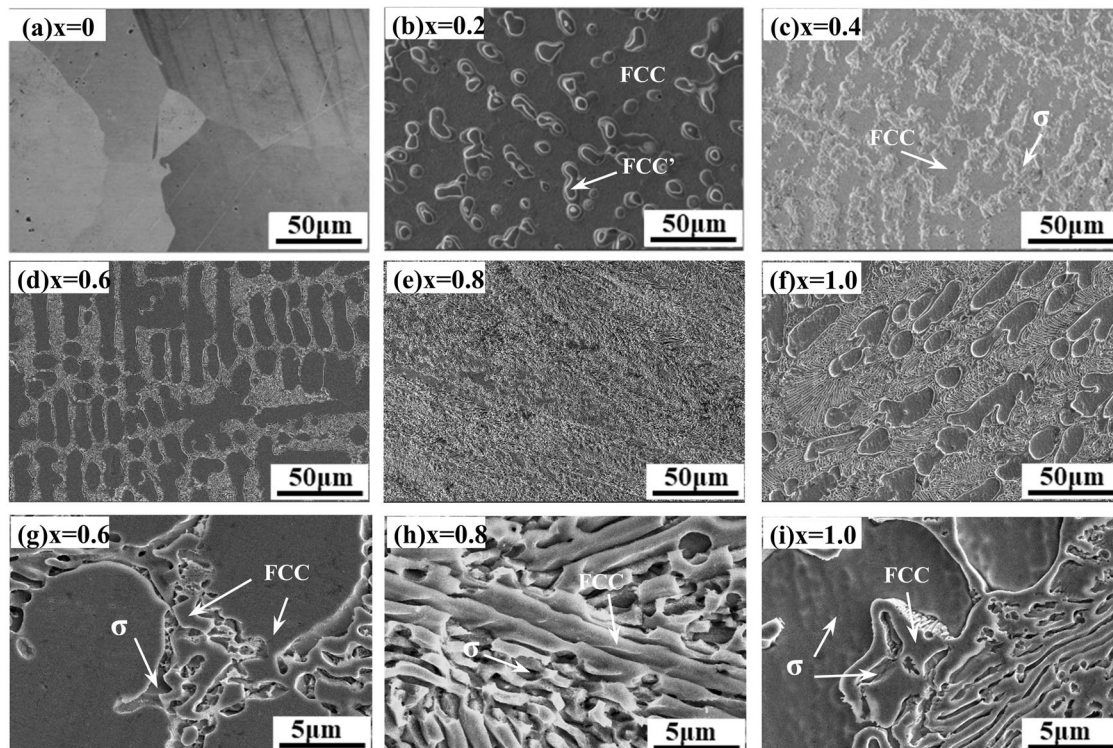
Fig. 2 SEM images of CoCrFeNiMo$_x$ HEAs. SEM images of **a** Mo$_0$, **b** Mo$_{0.2}$, **c** Mo$_{0.4}$, **d** and **g** Mo$_{0.6}$, **e** and **h** Mo$_{0.8}$, **f** and **i** Mo$_1$.
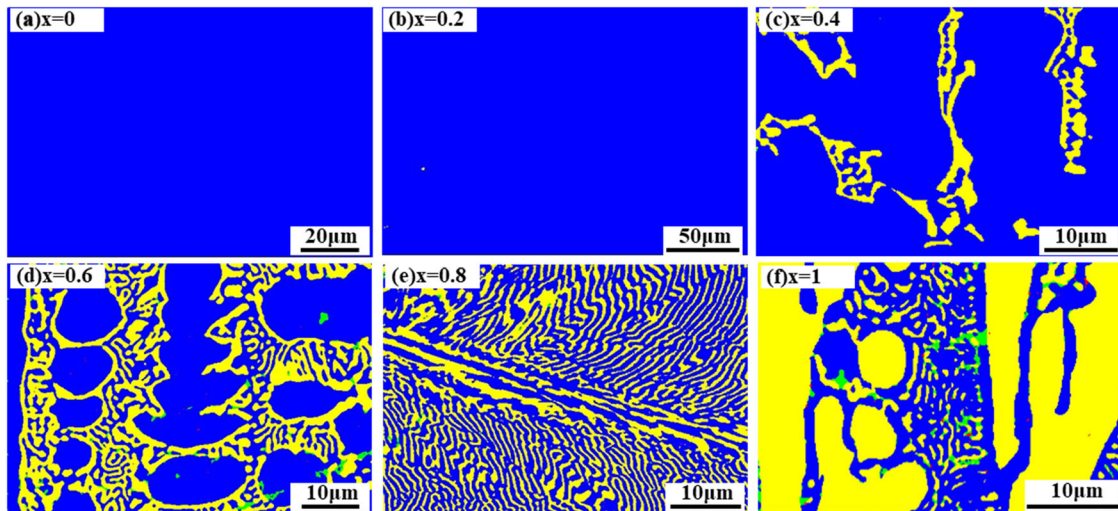
Fig. 3 Phase maps of the EBSD of CoCrFeNiMo$_x$ HEAs. Phase maps of **a** Mo$_0$, **b** Mo$_{0.2}$, **c** Mo$_{0.4}$, **d** Mo$_{0.6}$, **e** Mo$_{0.8}$, **f** Mo$_1$, the blue in the phase map stands for the FCC phase, the yellow stands for the σ-phase, and the green stands for unrecognized area.

Table 1. Chemical compositions for each phase of CoCrFeNiMo$_x$ ($x = 0.4, 0.6, 0.8$ 1) HEAs (at. %).

Alloy	Phase	Cr	Fe	Co	Ni	Mo
Mo$_{0.4}$	Nominal	22.73	22.73	22.73	22.73	9.08
	FCC matrix	22.35	23.53	23.40	23.34	7.37
	σ-phase	26.33	18.47	19.22	14.47	21.50
Mo$_{0.6}$	Nominal	21.74	21.74	21.74	21.74	13.04
	FCC matrix	19.9	22.38	22.58	24.40	10.74
	σ-phase	24.13	18.74	19.15	15.76	22.22
Mo$_{0.8}$	Nominal	20.83	20.83	20.83	20.83	16.68
	FCC matrix	19.01	21.95	21.69	23.46	12.92
	σ-phase	23.01	18.46	19.31	16.62	22.61
Mo$_1$	Nominal	20	20	20	20	20
	FCC matrix	18.12	22.23	21.53	24.6	12.52
	σ-phase	22.08	18.25	18.52	15.54	25.61

With the further increase of Mo content, the microstructure of the alloy changes from eutectic structure to hypereutectic structure in Mo$_1$ HEAs (Fig. 2f, i), and the FCC phase is no longer the main phase (Fig. 3f). According to SEM patterns and XRD analyses, it can be concluded that the σ-phase enriched Cr and Mo gradually precipitate from the CoCrFeNiMo$_x$ HEAs with the increase of Mo.

Electrochemical measurements

Figure 4a, b displays the polarization curves of as-cast CoCrFeNi-Mo$_x$ HEAs in 5 mM H$_2$SO$_4$ solution at room temperature. All the alloys exhibit a transition from active to passive behavior, with a wide passivation range and low current density, indicating that protective passive films can be formed on the surface of these alloys. Table 2 summarizes the corrosion current density (i_{corr}), corrosion potential (E_{corr}), and the passivation current density (i_{pass}) of all alloys. The i_{pass} is the current density at 0.4 V$_{SCE}$ in the middle of the passivation range. With the Mo content increased from 0.2 to 0.4, E_{corr} negatively shifts and the i_{corr} gradually increases, which shows the deterioration of corrosion resistance. However, a low i_{pass} of 0.874 μA cm^{-2} and a positive E_{corr} is observed in the Mo$_{0.6}$ showing the improvement of corrosion resistance. Then, the performance of Mo$_{0.8}$ and Mo$_1$ deteriorates again. In the passivation range, the level of i_{pass} reflects the

dissolution of the oxide film. The smaller i_{pass} of the oxide film, the better the stability of the film[19]. The i_{pass} of Mo$_{0.4}$, Mo$_{0.8}$, and Mo$_1$ increases gradually, indicating the poor stability of passive films. The lower i_{pass} in Mo$_{0.6}$ and Mo$_{0.2}$ suggests the higher stability of oxidation film on the surface, which is also in accordance with the higher corrosion resistance. Moreover, the current density of the HEAs with Mo addition decreases in the middle of the passivation range, especially in Mo$_{0.6}$, which may be attributed to the formation of molybdenum hydroxide or molybdate on the surface. And its adsorption enhances the passivation effect[23]. But the overall corrosion resistance of the alloy is still affected by microstructure, specifically the phase composition and distribution. Accordingly, the performance of Mo$_{0.8}$ and Mo$_1$ deteriorates.

The current density versus time plots at 0.4 V$_{SCE}$ are also provided to have a better insight into the passivation process (Fig. 4c, d). At the initial stage, the current density after potentiostatic polarization (i_p) decreases sharply, attributed to metal surface dissolution and the formation of passive film[24,25]. Then, the current remains relatively stable with extending polarization time, indicating that the formation and dissolution of the passive film have reached a balance after 10 h of potentiostatic polarization. For Mo$_{0.4}$, there are some sudden increases in local current density at the initial stage of potentiostatic polarization, which reflects the formation and annihilation of metastable pits on the surface. It indicates that local surface dissolution is obviously accelerated, the passivation ability of the surface is insufficient, and the protection of the generated oxide is insufficient. The higher i_p of alloys containing Mo than Mo$_0$ indicates a high dissolution rate on the surface of these alloys, which is associated with Cr, Mo-depletion regions caused by the second phase enriched in Mo and Cr[26]. Especially, the i_p of Mo$_1$ increases after half an hour of polarization, which indicates that the surface passive film is dissolved, which is consistent with the fact that there is no stable passivation range in the dynamic polarization curve. The order of i_p from large to small is Mo$_1$, Mo$_{0.8}$, Mo$_{0.4}$, Mo$_{0.6}$, Mo$_{0.2}$, Mo$_0$, and the corrosion resistance increases in turn, which is consistent with the potentiodynamic polarization results. In view of the abnormal phenomenon that the corrosion resistance of Mo$_{0.6}$ is higher than Mo$_{0.4}$, the phase structure and passive film composition will be discussed later.

EIS measurements were conducted to further investigate the corrosion resistance of as-cast CoCrFeNiMo$_x$ HEAs. The Nyquist plots and Bode plots of the original alloys in the H$_2$SO$_4$ solution are illustrated in Fig. 5a, b. Nyquist plots shown in Fig. 5a are
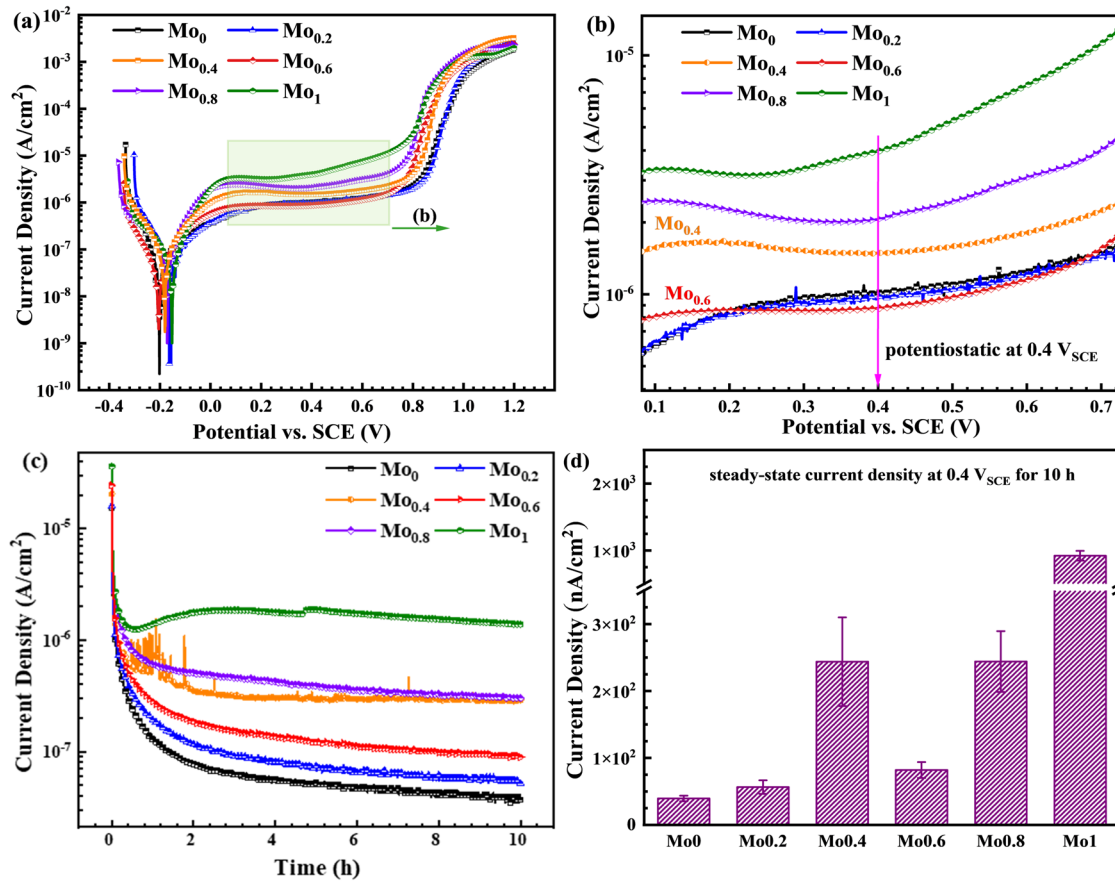
Fig. 4 Potentiodynamic and potentiostatic polarization results. a potentiodynamic polarization curves, **b** the enlarged region showing passive potential window, **c** potentiostatic polarization curves, **d** corresponding steady-state currents at 0.4 V_{SCE} for 10 h, the standard deviations (error bars) of the three tests for the steady-state currents.

Table 2. Key parameters from potentiodynamic polarization of CoCrFeNiMo$_x$ HEAs in 5 mM H$_2$SO$_4$ solution.

	i_{corr} (nA cm^{-2})	i_{pass} (μA cm^{-2})	E_{corr} (mV$_{SCE}$)	E_{pp} (mV$_{SCE}$)	E_b (mV$_{SCE}$)	ΔE (mV$_{SCE}$)
Mo$_0$	47	0.98	245	113	915	802
Mo$_{0.2}$	57	0.96	161	137	932	795
Mo$_{0.4}$	91	1.49	180	130	891	761
Mo$_{0.6}$	33	0.87	204	205	873	668
Mo$_{0.8}$	101	2.06	171	117	859	742
Mo$_{1.0}$	82	3.97	152	111	855	744

characterized as unfinished semi-arcs relating to the difference in passive film properties[27]. The corrosion resistance of alloys can be evaluated by the diameter of semi-arc in Nyquist plots. The larger diameter of the semi-arc, the better the corrosion resistance[28]. The semi-arc diameter of Mo$_{0.6}$ and Mo$_0$ HEA is significantly larger than that of other alloys, indicating a higher corrosion resistance of the two alloys. In the Bode plot (Fig. 5b), the impedance moduli display a good linear relationship with a slope close to −1 in the frequency range of $10^{-2} \sim 10$ Hz. Meanwhile, the phase angles of all the specimens reached the maximum in this frequency region, indicating the pseudocapacitive nature of the passive films on the CoCrFeNiMo$_x$ HEAs[29]. Furthermore, the value of |Z| in the Bode plot at 0.01 Hz usually corresponds to the polarization resistance reflecting the corrosion resistance of the alloy[30]. Compared with other CoCrFeNiMo$_x$ HEAs, the Mo$_{0.6}$ and Mo$_0$ HEAs have a higher |

Z| and larger phase angles at low frequency, showing better corrosion resistance.

The electrical equivalent circuit used for fitting the experimental data has also been inserted in Fig. 5a. This model is often adopted for a non-uniform passive film, which consists of a porous outer layer and a compact inner layer[31]. The R_s represents the solution resistance, $R_1//Q_1$ represents the electrical resistance and the capacitance of the outer layer, and $R_2//Q_2$ represents the equivalent resistance and capacitance of the inner layer[31–33]. Considering the rough electrode surface or uneven surface current, Q is used to signify the possibility of a non-ideal capacitance (CPE). It can be defined by the following Eq. (1)[34]

$$Z_{CPE} = \frac{1}{Y_0}(j\omega)^{-n} \tag{1}$$

Where Y_0 is the modulus, ω is the angular frequency, $j^2 = -1$ is the imaginary number and n is the CPE exponent. When $n = 1$, the CPE is considered an ideal capacitor, and non-ideal when $0.5 < n < 1$.

Equivalent electrical circuits were employed to analyze the EIS data, as shown in Fig. 5c, d and Table 3. For all HEAs, R_2 is significantly higher than R_1, and Q_1 is higher than Q_2, which is close to 1, showing a denser inner film and loose outer film. The low R_1 can be ascribed to the low stability of some metal oxide species such as Fe-oxide which has poor stability and might selective dissolution in acidic solutions with low pH[32]. But the presence of stable elements such as Cr- and Mo-based ions will maintain surface adsorption[30,35], resulting in the formation of an external porous layer. The impedance R_2 of the inner passive film can be used as an effective index to evaluate the corrosion

Table 3. The fitted parameters for EIS of the as-cast CoCrFeNiMo$_x$ HEAs in 5 mM H$_2$SO$_4$ solution.

	Mo$_0$	Mo$_{0.2}$	Mo$_{0.4}$	Mo$_{0.6}$	Mo$_{0.8}$	Mo$_{1.0}$
R_s (Ω cm^2)	88	93	91	79	93	42
$Q_1 - Y_0$ (× Ω^{-5} cm^{-2} s^n)	13.0	14.0	36.0	20.0	16.0	45.0
n_1	0.84	0.85	0.80	0.83	0.86	0.84
R_1 (kΩ cm^2)	35	45	63	27	26	56
$Q_2 - Y_0$ (× Ω^{-5} cm^{-2} s^n)	6.6	9.1	8.3	9.0	17.0	21.0
n_2	0.98	1	0.96	1	1	1
R_2 (kΩ cm^2)	1000	960	340	670	120	103
χ^2	8.2×10^{-5}	8.2×10^{-5}	1.0×10^{-4}	2.8×10^{-4}	9.7×10^{-5}	4.0×10^{-4}
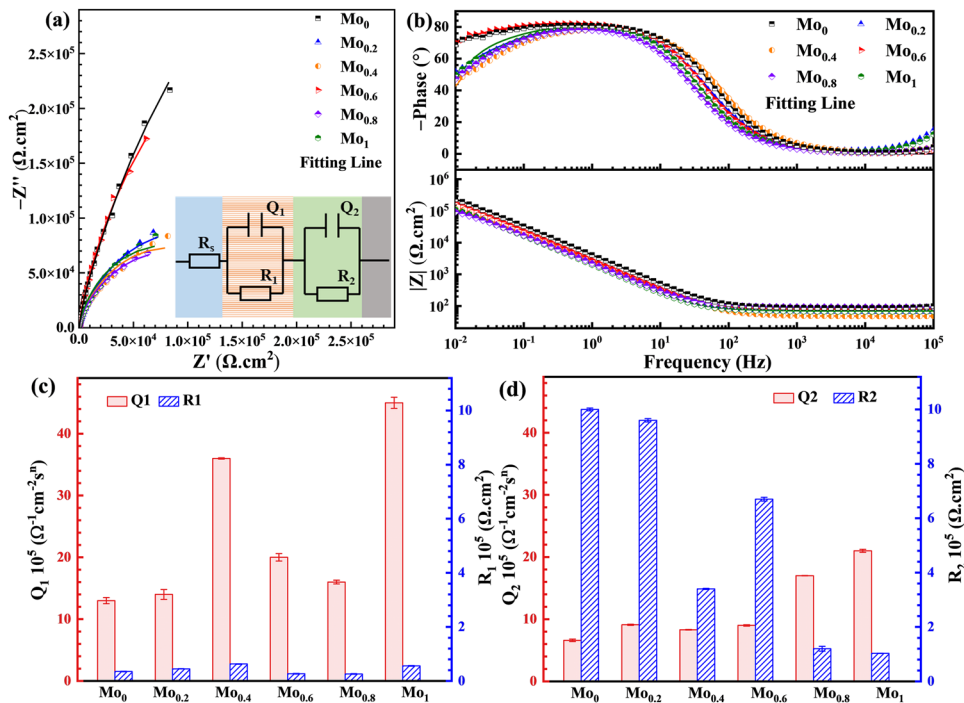
Fig. 5 EIS measurements in 5 mM H$_2$SO$_4$ solution. a Nyquist plots, **b** Bode plots, **c, d** the variation of fit resistance and capacitance, the standard deviations (error bars) of the three tests for Q_1, Q_2, R_1, R_2.

resistance of the alloy. As shown in (Fig. 5d, R_2 decreases with the increase of Mo content but rises at $x = 0.6$, indicating a better corrosion resistance of Mo$_{0.6}$ than that of Mo$_{0.4}$, Mo$_{0.8}$, and Mo$_1$. The increase in Q_2 over Mo contents shows that the addition of Mo leads to great changes in the thickness and composition of the passive film[36,37]. The Q_2 of Mo$_{0.8}$ and Mo$_1$ HEAs is larger (Fig. 5d), which may be due to the increase of capacitance caused by the decrease of electron dissipation layer thickness and the increase of carrier number[9,32], resulting in the deterioration of corrosion resistance of these two alloys.

The semiconducting properties of the passive films formed on as-cast CoCrFeNiMo$_x$ HEAs were characterized by the Mott–Schottky analysis. According to the Mott–Schottky plots, the potential-capacitance relationship in the space charge layer under the depletion condition can be expressed through Eq. (2):

$$\frac{1}{C^2} = \pm \frac{2}{e\varepsilon\varepsilon_0 N A^2}\left(E - E_{FB} - \frac{kT}{e}\right) \quad (2)$$

where e is the charge of a single electron (1.6×10^{-19} C), k is the Boltzmann constant (1.38×10^{-23} J K^{-1}), ε and ε_0 refer to the dielectric constant of the semiconductor (15.6), and the permittivity of vacuum (8.85×10^{-14} F m^{-1}), respectively. The E_{FB} is the potential of flat-band (V$_{SCE}$), which corresponds to the voltage intercept of the linear segment on the Mott–Schottky plots. T is the absolute temperature (K) and N represents the carrier density (cm^{-3}) including the donor concentration (N_D) and acceptor concentration (N_A).

Figure 6a shows the Mott–Schottky plots of the passive film on the CoCrFeNiMo$_x$ HEAs after the potentiostatic polarization in 5 mM H$_2$SO$_4$ solution at 0.4 V$_{SCE}$ for 10 h. All plots show two linear regions and a narrow flat region (–0.2~ 0.4 V$_{SCE}$), which contains flat-band potential E_{FB}. A similar phenomenon has been reported for the passive film formed on stainless steel[38]. At a potential lower than E_{FB}, the negative slope represents the p-type semiconductor corresponding to the outer layer of the passive film. While the positive slope at a potential higher than E_{FB} indicates the n-type semiconductor, which corresponds to
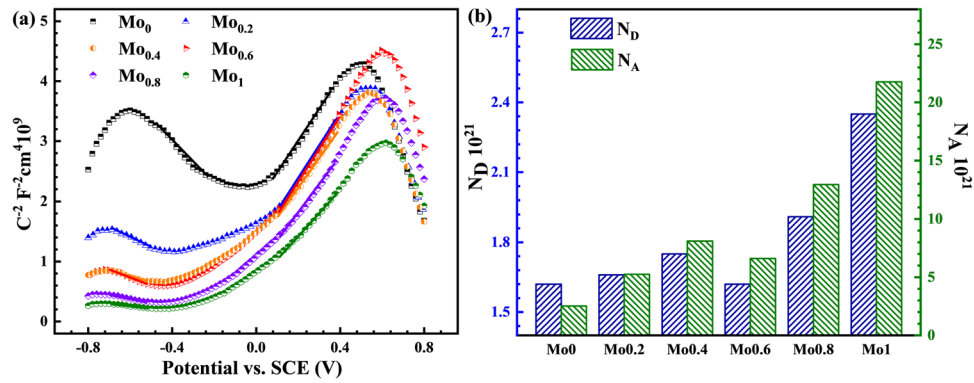
Fig. 6   Mott–Schottky results of the passive films. a Mott–Schottky plots of the passive film after the potentiostatic polarization at 0.4 V_{SCE} for 10 h, **b** The donor (N_D) and acceptor densities (N_A) of the n-type and p-type semiconductors.
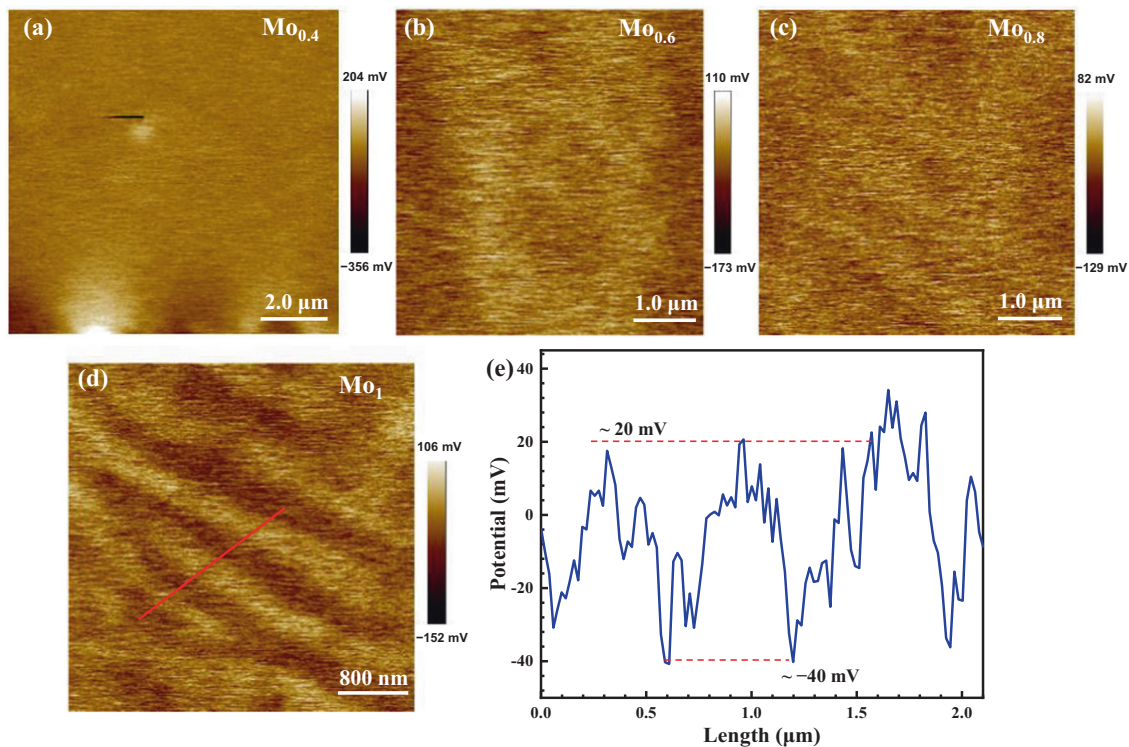

Fig. 7   SKPFM results of CoCrFeNiMo$_x$ HEAs. Surface voltage potential maps of (**a**) Mo$_{0.4}$, (**b**) Mo$_{0.6}$, (**c**) Mo$_{0.8}$, (**d**) Mo$_1$, (**e**) corresponding line-profile analysis of relative Volta potential in map (**d**).

the inner layer of the passive film[39]. The donor (N_D) and acceptor densities (N_A) of the passive films formed on CoCrFeNiMo$_x$ HEAs were calculated and shown in Fig. 6b. All carrier densities are in the range of $10^{21} \sim 10^{22}$ cm^3, which presents a similar passive film character to that of the stainless steels[40–42]. Particularly, the N_A of all CoCrFeNiMo$_x$ HEAs is an order of magnitude larger than N_D, indicating the dense inner layer (n-type) and the loosened outer layer (p-type). In addition, with the addition of Mo, the carrier densities increase gradually, indicating the deterioration of the corrosion resistance of the alloy. The carrier concentration of Mo$_0$, Mo$_{0.2}$, and Mo$_{0.6}$ are low, showing better corrosion resistance. The carrier densities of Mo$_{0.8}$ and Mo$_1$ HEAs are higher than that of other alloys, suggesting more defects in the passive film. and higher electrochemical activity at the solution-metal interface, which is consistent with the previous electrochemical test results.

The selective dissolution of alloys

To confirm the electrochemical potential difference between FCC and σ-phase, Volta potential maps were acquired by SKPFM for the alloys, as indicated in Fig. 7. The bright area demonstrates more positive potential than the dark area in the SKPFM images. The precipitated σ-phase shows a larger Volta potential value (~20 mV) than the FCC phase (~ −40 mV), as shown in Fig. 7d. Undoubtedly, the Volta potential difference leads to micro-galvanic activity between the σ-phase and FCC phase, at which the latter acts as the micro-anode to erode preferentially whilst σ-phase acts as the micro-cathode[43,44]. However, the Volta potential difference between these two phases depends on the Mo content. With the increase of Mo, the Volta potential difference increases gradually, which means that the risen driving force for galvanic coupling between those regions[45]. For Mo$_{0.4}$, there is no obvious Volta potential difference between the two phases. And Volta potential difference over the σ-phase and FCC phase is low for
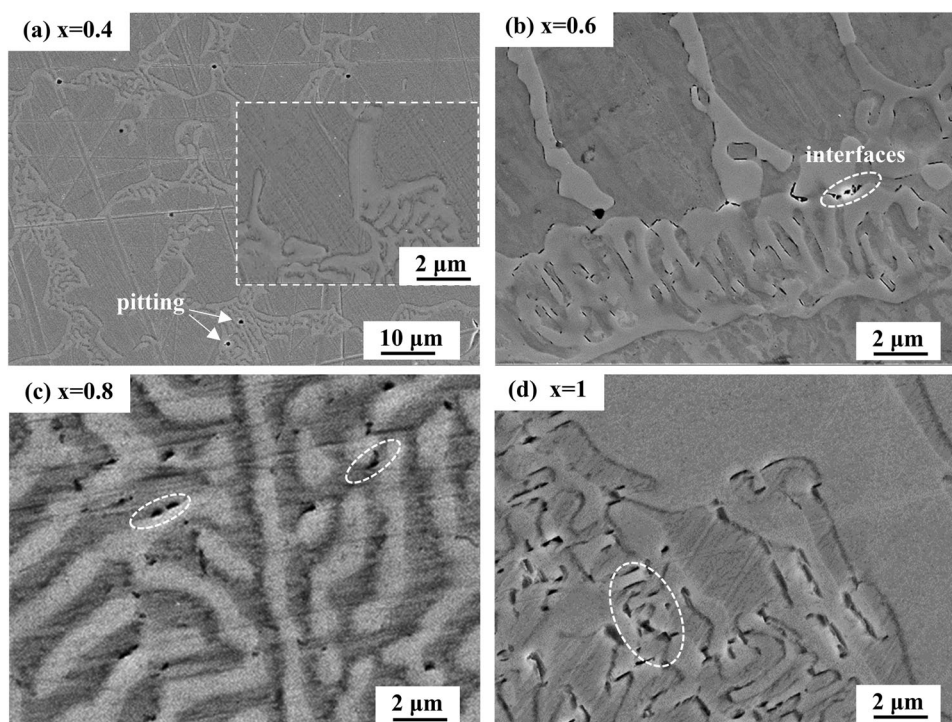
Fig. 8 SEM images after the potentiostatic polarization. SEM images of (**a**) $Mo_{0.4}$, (**b**) $Mo_{0.6}$, (**c**) $Mo_{0.8}$, (**d**) Mo_1 after the potentiostatic polarization at 0.4 V_{SCE} for 10 h.

$Mo_{0.6}$ and $Mo_{0.8}$ alloys. But in the following observation of corrosion morphology, these three alloys still show weak galvanic corrosion. For the Mo_1, the Volta potential difference is about 60 mV at the interface between the σ-phase and FCC phase, which may be attributed to the quite different proportion of the two phases in the hypereutectic structure. The increased Volta potential difference indicates the enhanced micro-galvanic corrosion in Mo_1 alloy[43]. The aggravated selective corrosion makes Mo_1 show higher i_p and poor corrosion resistance in electrochemical tests. Nevertheless, the 60 mV Volta potential difference is relatively low and only shows the relatively weak micro-galvanic corrosion in $CoCrFeNiMo_x$ HEAs[43]. Meanwhile, the Volta potential difference will affect the formation of the passive films on the surface of the alloys, the corresponding discussion comes later.

Microstructural characterization also was conducted to support the selective corrosion of the FCC matrix (Fig. 8). The pitting occurs on the $Mo_{0.4}$ alloy surface (Fig. 8a). With the content of Mo in the alloy more than 0.4, the main corrosion way of the alloy changes into gradually enhanced galvanic corrosion. The secondary electron images show that there is an obvious contrast difference between the two phases, indicating that the FCC phase with darker color tends to dissolve. For the $Mo_{0.6}$, the corrosion type appears as galvanic corrosion at the interfaces between FCC matrix and σ-phase, as shown in Fig. 8b. In $Mo_{0.8}$ eutectic alloy, the increase of phase interface provides more preferential corrosion areas (Fig. 8c), which leads to the deterioration of corrosion resistance. And with increasing Mo content, the Volta potential difference increases, especially for Mo_1. As a result, the corrosion at the two-phase interface is particularly aggravated in Fig. 8d. In summary, when σ-phase appears, the FCC matrix is selectively dissolved. And with the increase of Mo content, the galvanic corrosion of the two-phase interface gradually intensified.

The composition and structure of passive films
Figure 9 shows the depth profiles of the Cr, Co, Ni, O, Fe, and Mo elements in the passive films of as-cast $CoCrFeNiMo_x$ HEAs after

the potentiostatic polarization at 0.4 V_{SCE} for 10 h in 5 mM H_2SO_4 solution. The amount of O and Cr is higher than other elements during the initial stage of sputtering. With the increase of sputtering time, the amount of O and Cr decreases gradually, indicating that Cr-enrich passive film is formed on the surface of each alloy. The inner layer and outer layer of the passive film are divided by the highest point of Cr content. When the differential of Cr content versus time is always greater than −3, it means that the Cr content tends to be stable and the sputtering reaches the substrate. The atomic ratio of Fe, Co, and Ni increases with the sputtering, suggesting that the three elements are selectively dissolved and have limited contribution to the passive film[46,47]. The selective dissolution of these elements leads to the formation of a Cr-enrich passive film, which is similar to the passivation of stainless steel[9].

Figure 9g compares the O content of each HEA. The content of O increases with the addition of Mo, indicating an increased amount of metal oxides and hydroxides in the passive film. The surface O content of Mo_1 is higher than other alloys. Combined with the high carrier densities, the surface electrochemical activity of Mo_1 is higher, which may lead to the accumulation of a larger number of loose corrosion products[48]. As shown in Fig. 9h, the atomic ratio of Cr in Mo_0 gradually decreases with the increase of sputtering time. In the alloys containing Mo, the peak value of the atomic ratio of Cr appears in the sub-surface layer of the passive film. The more Mo content is, the more obvious this phenomenon is. This is due to the selective dissolution of the primary phase caused by the precipitation of the second phase, which may cause the loss of surface Cr and nonuniform distribution of Cr in the passive film[18]. In particular, in the passive film formed on $Mo_{0.8}$ and Mo_1, Cr has a sudden change in the depth direction. The decrease of Cr content in the outer passive film and the nonuniform distribution of Cr will have a negative impact on the corrosion resistance. At the same time, the more selective dissolution of Ni, Cr, and Fe due to the enhanced selection corrosion, may lead to the reduction of the densification of the passive films. In particular, the content of Cr in the surface layer of
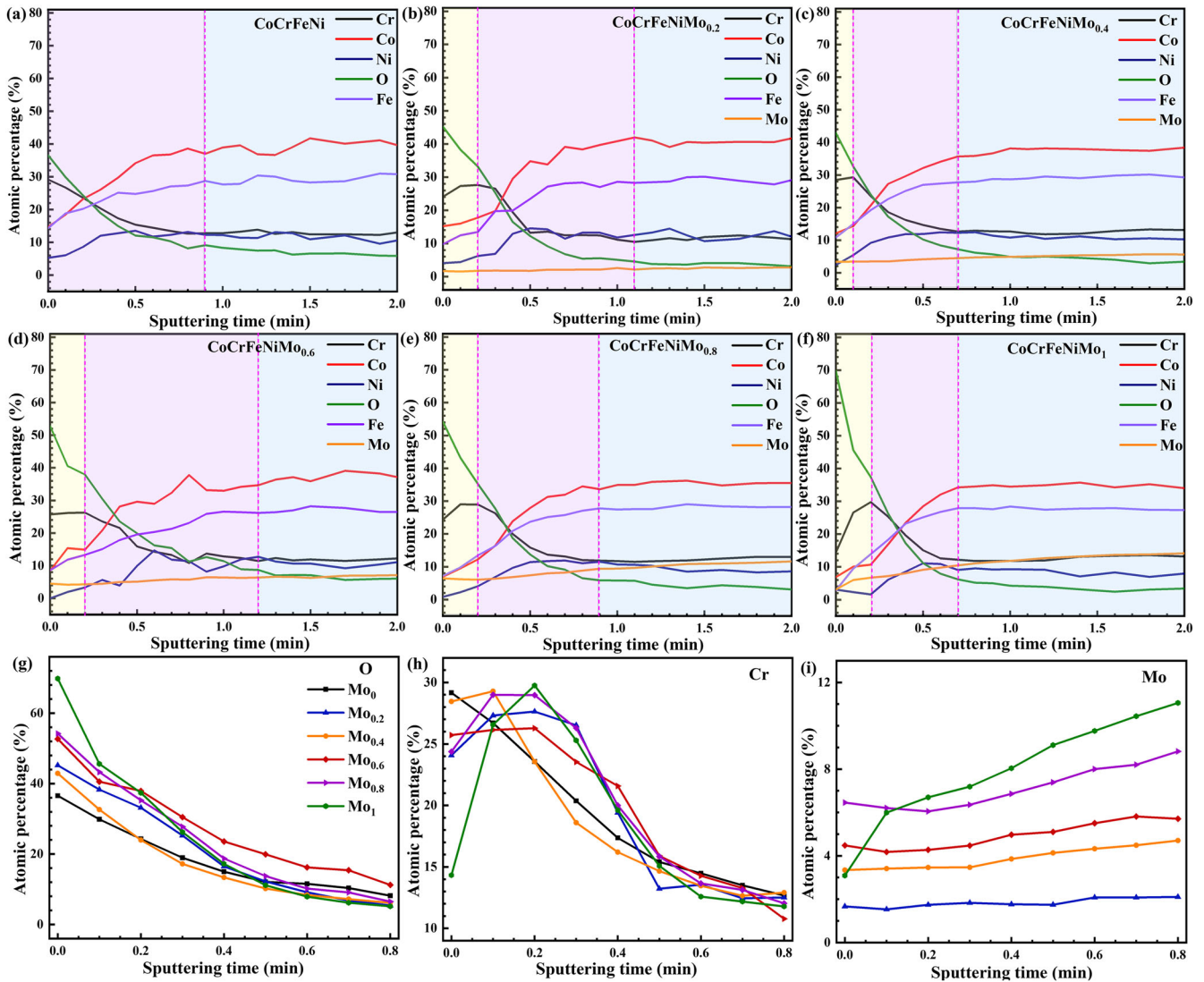
Fig. 9 XPS depth profiles of the elements in the passive films. XPS depth profiles of the elements in the passive film after the potentiostatic polarization at 0.4 V_{SCE} for 10 h in 5 mM H_2SO_4 solution, **a** Mo_0, **b** $Mo_{0.2}$, **c** $Mo_{0.4}$, **d** $Mo_{0.6}$, **e** $Mo_{0.8}$, and **f** Mo_1, as well as the comparison in element **g** O, **h** Cr, and **i** Mo distribution.

$Mo_{0.6}$ is stable, indicating that the distribution of Cr in the passive film is uniform, therefore, the passive film has good stability. The content of Mo increases slightly with the increase of sputtering time as shown in Fig. 9j, and the upward trend is more obvious in Mo_1 HEAs than in other alloys. Furthermore, the changing trend of Mo content shows that Mo tends to dissolve rather than passivate in the alloy passive film with a molar ratio greater than 0.6.

Further analyses of O, Cr, and Mo spectra were performed and provided in Figs. 10–12 to determine the depth distribution of the species with different oxidation states. As shown in Fig. 10, the O 1s spectra were characterized by the presence of three components O^{2-} (530.7 eV), OH^- (532.5 eV), and H_2O (532.8 eV). The $Mo_{0.2}$ (Fig. 10a), $Mo_{0.4}$ (Fig. 10b), $Mo_{0.6}$ (Fig. 10c), and Mo_1 (Fig. 10d) are selected for analysis. The Mo_0 and $Mo_{0.8}$ are shown in Supplementary Fig. 3. The intensity of O1s spectra decreases gradually with the increase of sputtering time. And except for Mo_1, the peak of O^{2-} is the main peak in the O 1s spectra of other alloys. It shows that the passive films with alloy oxides as the main component are formed on the surface of the alloys (Supplementary Fig. 2a). The spectral intensity of O^{2-} in $Mo_{0.2}$ and $Mo_{0.6}$

decreases slowly in the depth direction of the passive films (Fig. 10a, c). When the sputtering time is 30 s, there is still an obvious oxide peak. The oxide content of $Mo_{0.6}$ is always higher than $Mo_{0.4}$, inferring that more metal oxides in the passive film lead to its corrosion resistance better than $Mo_{0.4}$. In addition, Mo_1 shows a different spectrum (Fig. 10b). When the sputtering time is 6 s, the hydroxide is the main specie, which is more than that of other alloys.

According to the fitting results, Fig. 13a displays the ratio of O^{2-}/OH^- with increasing depth. $Mo_{0.6}$ has a stable and highest ratio of O^{2-}/OH^-, indicating that its passive film is relatively uniform and dense. In addition, Mo_1 provides a higher ratio of O^{2-}/OH^- after 4 cycles. However, the ratio of O^{2-}/OH^- changes sharply, and the ratio of the surface layer film is lower than other alloys, suggesting that the outer layer of the passive film is mainly composed of loose metal hydroxide, which cannot resist corrosive ions, resulting in poor corrosion resistance of Mo_1.

The Cr $2p_{3/2}$ spectra were separated into $Cr(OH)_3$ (578.7 eV), Cr_2O_3 (576.5 eV), and Cr^0 (574.4 eV) (Fig. 11). the $Mo_{0.2}$ (Fig. 11a), $Mo_{0.4}$ (Fig. 11b), $Mo_{0.6}$ (Fig. 11c), and $Mo_{0.8}$ (Fig. 11d) are selected.
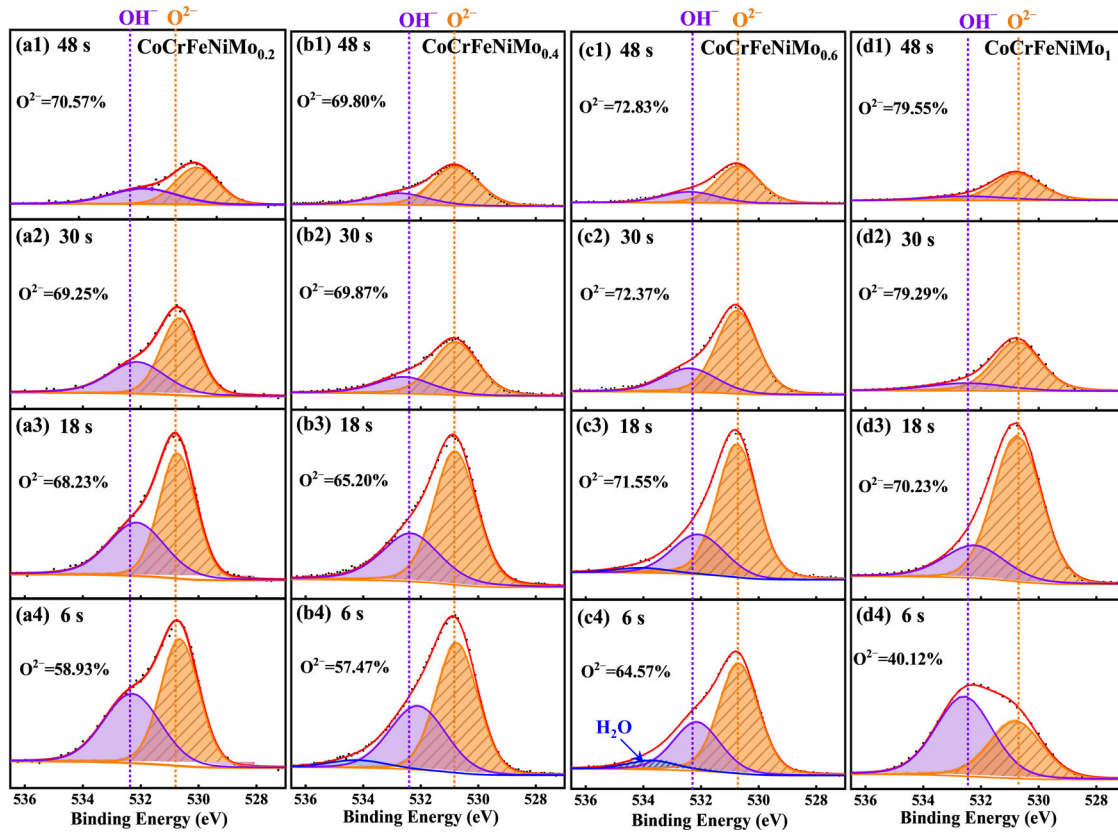
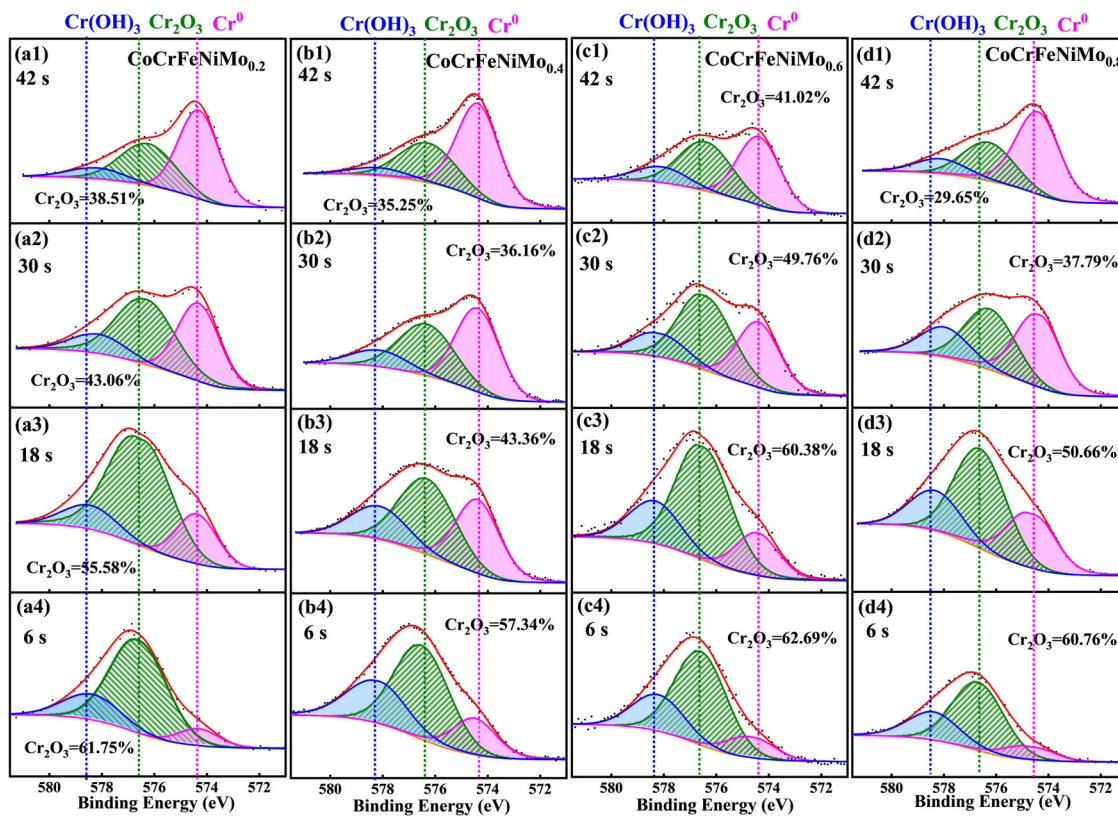Fig. 10   The detailed XPS spectra of O 1 s of the passive films. a Mo$_{0.2}$, b Mo$_{0.4}$, c Mo$_{0.6}$, and d Mo$_1$ HEAs.
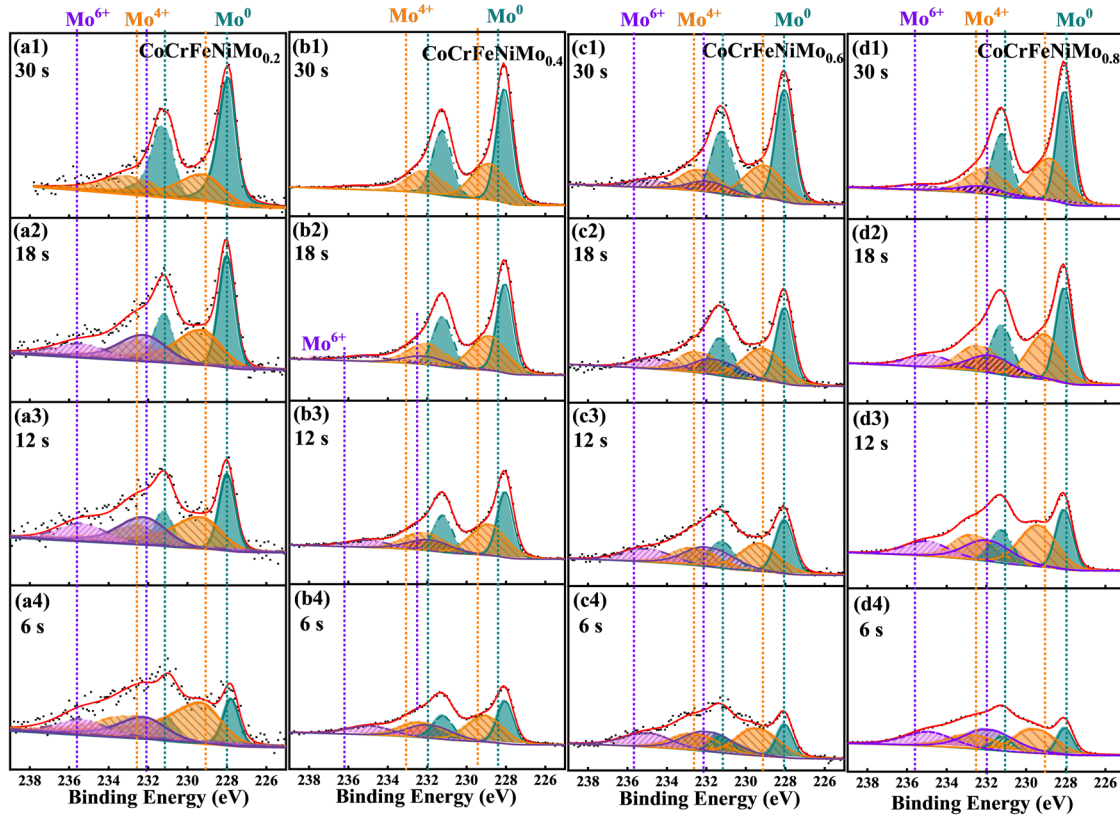

Fig. 11   The detailed XPS spectra of Cr 2p$_{3/2}$ of the passive films. a Mo$_{0.2}$, b Mo$_{0.4}$, c Mo$_{0.6}$, and d Mo$_{0.8}$ HEAs.

Fig. 12   The detailed XPS spectra of Mo 3d of the passive films. a $Mo_{0.2}$, **b** $Mo_{0.4}$, **c** $Mo_{0.6}$, and **d** $Mo_{0.8}$ HEAs.
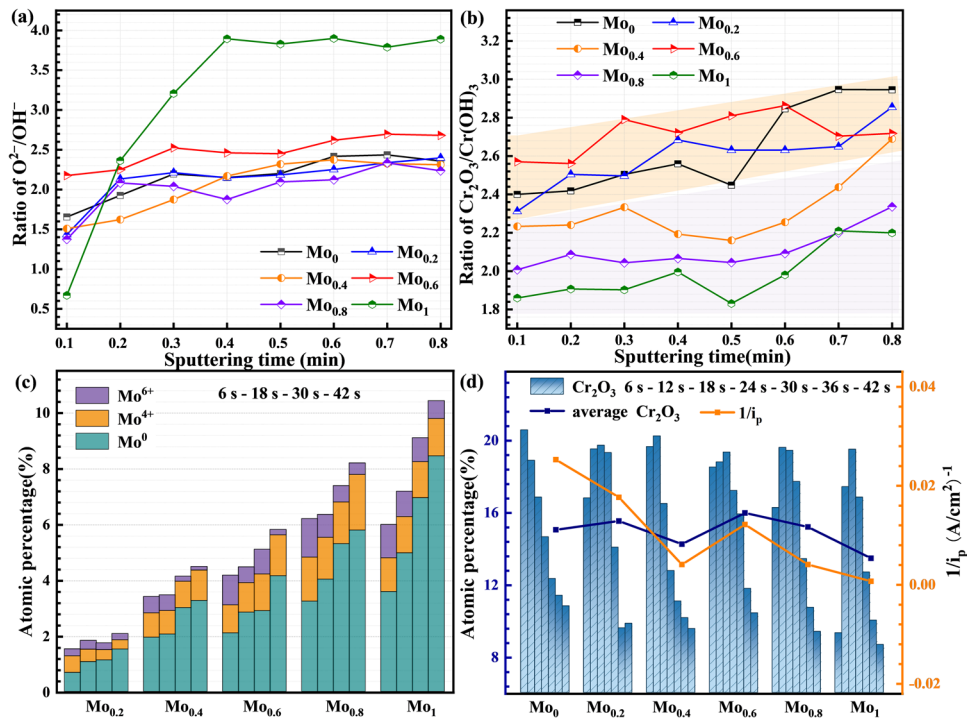
Fig. 13   Special species distribution summarized from XPS depth profiles. a XPS depth profiles of the ratio of O^{2-}/OH^-, **b** the ratio of Cr_{ox}/Cr_{hy}, **c** the atomic percentage of Mo species, **d** the atomic percentage of Cr_2O_3 for the passive films and reciprocal of passivation current density.
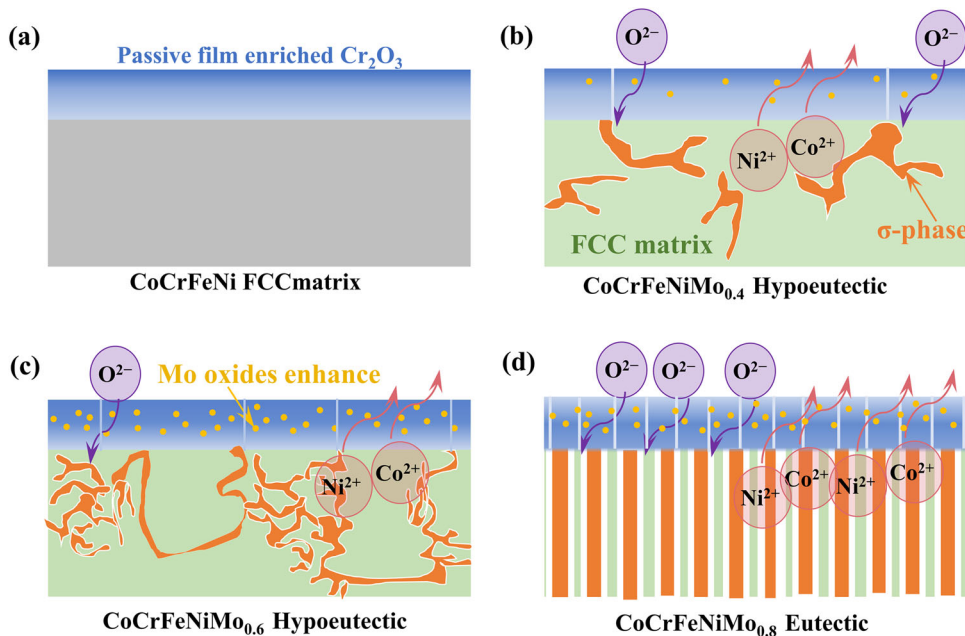
Fig. 14 The schematic diagram of galvanic corrosion and passivation. a Mo_0, **b** $Mo_{0.4}$, **c** $Mo_{0.6}$, and **d** $Mo_{0.8}$ HEAs.

The Mo_0 and Mo_1 are shown in Supplementary Fig. 3. Cr element exhibits the special property to combine a relatively high heat of adsorption of oxygen (or OH^-) with a relatively low Cr-Cr bond strength, which is a crucial factor for the nucleation of the oxide[49]. In addition, compared to $Cr(OH)_3$, Cr_2O_3 has a more thermally stable anhydrous structure and lower point defect density[50], so it plays an important role in corrosion resistance. With the increase of sputtering time, the main peak of Cr gradually moves from $Cr(OH)_3$ and Cr_2O_3 with binding higher energy to Cr metal with lower binding energy (Supplementary Fig. 2b). In the passive films, Cr_2O_3 is the main species of Cr. When the time increases to 30 s and 42 s, the percentage of Cr_2O_3 in the spectrum of $Mo_{0.2}$ and $Mo_{0.6}$ is always higher than that in $Mo_{0.4}$ and Mo_1 indicating that Cr_2O_3 is deeply and evenly distributed in the passive film, which makes the passive films of $Mo_{0.2}$ and $Mo_{0.6}$ have good stability.

According to the XPS analysis results, the ratio of Cr_2O_3 and $Cr(OH)_3$ (Cr_{ox}/Cr_{hy}) for the passive films formed on $CoCrFeNiMo_x$ is shown in Fig. 13b. $Mo_{0.6}$, $Mo_{0.2}$, and Mo_0 have a high ratio of Cr_{ox}/Cr_{hy}. And the passive films contain more Cr_2O_3, which can well protect the alloys and have good corrosion resistance. The ratio of Cr_{ox}/Cr_{hy} for $Mo_{0.4}$, $Mo_{0.8}$, and Mo_1 decrease in turn, which corresponds to the gradually decreased corrosion resistance and is consistent with the results of the electrochemical test. It can be concluded that the content of Cr_2O_3 in the passive film is the decisive factor affecting the corrosion resistance.

The Mo 3d spectra were separated into Mo^{6+} (235.5 and 232.2 eV), Mo^{4+} (232.5 and 229.0 eV), and Mo^0 (231.1 and 228.0 eV) (Fig. 12). The behavior of Mo 3d spectra are similar to the Cr $2p_{3/2}$ spectra, with the increase of sputtering time, the metal peak increases, and the peaks of metal oxides decrease (Supplementary Fig. 2d). The content of high valence Mo^{6+} oxides gradually decreases with the increase of Mo and disappears in $Mo_{0.2}$ after a sputtering time of 30 s. With the increase of Mo content, the higher valence oxide of Mo appears in deeper passive films, and the proportion gradually increases in $Mo_{0.6}$ (Fig. 12c1), $Mo_{0.8}$ (Fig. 12d1), and Mo_1 (Supplementary Fig. 3e1). Figure 13c shows the atomic percentage of Mo in different valence states. With the increase of sputtering time, the content of Mo metal increases, and the Mo oxides including Mo^{6+} and Mo^{4+} contents decrease gradually. Moreover, with the molar ratio of Mo increasing from 0.4 to 0.6, the content of the oxides Mo^{6+} and Mo^{4+} increases

gradually. With the increase of Mo content to more than 0.6, the percentage of Mo oxides remains stable, indicating that the oxides of Mo don't increase with the increase of Mo content in the alloy, and there is an upper limit for the oxide species of Mo in the passive film. This may be attributed to a large amount of energy released upon adsorption of oxygen not easily disrupting a large number of Mo-Mo bonds[49]. Because the transition from adsorbed overlayer to oxide nucleation requires the disruption of metal-metal bonds[49]. Previous studies have shown that Mo oxides have a positive effect on the passive film[18,51], but the positive effect is limited due to the limitation of Mo oxides contents.

The role of Mo in microstructure and passive films
In general, the addition of Mo has a negative impact on the corrosion resistance of the alloy, with a relatively small negative impact on $Mo_{0.2}$ and $Mo_{0.6}$. Especially, the corrosion resistance of Mo_0 is better than other alloys (Figs. 4 and 5), but its Cr_2O_3 content is not higher than that of other alloys (Fig. 13d). On the one hand, Mo_0 is a single-phase structure with uniform composition, which is easy to form a uniform and dense passive film (Fig. 14a). On the other hand, the fact that Cr_2O_3 content in other alloys does not decrease significantly may be attributed to Mo promoting the enrichment of Cr_2O_3 in the passive film, and the selective dissolution of other elements promoted by phase selective corrosion. However, The Cr_2O_3 passive film formed by the massive dissolution of other elements is looser and less protective than the passive film formed by the diffusion and oxidation of Cr elements to the outer layer (Fig. 14). Therefore, the addition of Mo does not obviously change the percentage of Cr_2O_3 in the passive film, but the corrosion current density increases.

For $Mo_{0.2}$, the addition of a small amount of Mo contributes to the formation of Mo oxides in the passive film, and Cr_2O_3 is uniformly distributed in the passive film. There is no precipitated σ-phase in $Mo_{0.2}$ (Figs. 2 and 3), only elemental segregation of Mo, and thus very weak selective corrosion in the alloy structure. And Mo promotes the deprotonation of Cr hydroxide[52], resulting in a higher content of Cr_2O_3 in $Mo_{0.2}$ than that in Mo_0. In contrast, the element segregation caused by the addition of Mo will also slightly increase the current density in corrosion. The corrosion resistance of $Mo_{0.4}$ deteriorates (Fig. 14b) due to the noticeable decrease of Cr_2O_3 content (Fig. 13d), even though a few amounts

of Mo oxides are formed. More importantly, due to the precipitation of a small amount of discontinuous second phase rich in Mo and Cr, selective corrosion dissolution is conducted in the primary phase[18,51]. Therefore, the limited Mo and Cr oxides and selective corrosion make the worse corrosion resistance of $Mo_{0.4}$ than $Mo_{0.2}$ and $Mo_{0.6}$.

As the atomic ratio of Mo increases to 0.6 (Fig. 14c), the corrosion resistance of the alloy improves, which is better than $Mo_{0.4}$. Ameer et al. proposed that the oxides of Mo can eliminate the defects on the surface of the passive film, thereby improving the pitting resistance of the alloy[53]. The content of Mo oxides is more than $Mo_{0.4}$, which plays a synergistic effect in the passive film. In addition, Mo can promote the enrichment of Cr_2O_3 in the passive film, making the passive film contain a large amount of Cr_2O_3. The precipitation of a more connected second phase may alleviate the galvanic corrosion caused by pitting precipitation[51]. Under this composition, the increase of the Cr_2O_3 percentage caused by the addition of Mo reached the maximum value, and the protective effect of Cr_2O_3 dominates, rather than the corrosion resistance reduction caused by the selective dissolution. Hence, Mo has a little negative impact on the corrosion resistance of $Mo_{0.6}$.

When the content of Mo is greater than 0.8, the corrosion resistance of the alloy decreases, and the corrosion resistance of Mo_1 deteriorates sharply. $Mo_{0.8}$ is a typical lamellar eutectic structure (Fig. 14d). The lamellar structure will produce more phase boundaries, providing more preferential dissolution boundaries for corrosion, which will lead to the increase of corrosion current density (Fig. 8). From the composition of the passive film, with the further increase of the content of Mo to 0.8, the auxiliary Mo oxide did not increase compared with $Mo_{0.6}$ (Fig. 13c), while the content of Cr_2O_3 in the passive film decreased (Fig. 13d), leading to the decline of the quality of the passive film. The decrease in the percentage of Cr_2O_3 is mainly attributed to the high content of the decreasing diffusion of Cr to the outer layer of the passive film, making the outer layer of the passive film lose its protection, leading to the invasion of corrosive ions, which further worsens the protection of the passive film. The dissolution of Ni and other elements in $Mo_{0.8}$ due to the selective corrosion of the phase also reduces the density of the passive film. Mo_1 shows the high carrier density in the Mott–Schottky test and the high content of metal hydroxide in the passive film components in XPS analysis, indicating that there are a lot of defects in the passive film and the accumulation of corrosion products. The lower ratio of Cr and Mo of Mo_1 than that of other alloys leads to poor development of passive film and has poor stability and protection[54]. In addition, the proportion of two phases in hypereutectic structure is quite different, forming a large cathode and a small anode, which will cause serious corrosion of the FCC matrix. And the more different Volta potential than that of other alloys enhances the micro-galvanic corrosion.

In summary, the addition of Mo deteriorates the corrosion resistance of the CoCrFeNiMo$_x$ HEAs owing to the selective dissolution of the FCC matrix over the σ-phase. The preferential corrosion of phase interfaces amplifies in eutectic ($Mo_{0.8}$). And the increased Volta potential difference accelerate the micro-galvanic corrosion in hypereutectic structures (Mo_1). Mo promotes the enrichment of Cr_2O_3 in the passive film which enhances the corrosion resistance of the CoCrFeNiMo$_x$ HEAs. But the limited Mo and Cr oxides and selective corrosion reduce the corrosion resistance of $Mo_{0.4}$. And the poor passive films resulting from the aggravated phase selective corrosion offer limited protection for $Mo_{0.8}$ and Mo_1, resulting in poor corrosion resistance. In $Mo_{0.6}$, the percentage of Cr_2O_3 in the passive film increases to the maximum value due to the addition of Mo. The beneficial effect of Cr_2O_3 enrichment exceeds the negative impact of Mo-induced selective corrosion. As a result, $Mo_{0.6}$ exhibits a lower corrosion rate than that of $Mo_{0.4}$, $Mo_{0.8}$, and Mo_1.

METHODS

Materials preparation

The CoCrFeNiMo$_x$ ($x = 0$, 0.2, 0.4, 0.6, 0.8, and 1.0) HEAs were cast via arc melting of mixture of the pure metal elements (purity > 99.99 %) in a 0.01 atm vacuum. The ingots were cast and re-melted at least 5 times to facilitate composition homogenization. Samples with dimensions of $10 \times 10 \times 4$ mm were encapsulated by epoxy resin. Then, the only exposed surface of 1 cm^2 was ground sequentially from 600 to 2000 grit SiC paper. The EBSD samples were ground sequentially from 600 to 4000 grit SiC paper and were polished with silica polishing solution for 30 min. Finally, the specimens were cleaned with deionized water, alcohol and then dried in the cool air.

Electrochemical measurements

Corrosion behavior was carried out by an electrochemical workstation (Princeton PARSTAT 4000) using a conventional three-electrode electrochemical cell system, which consisted of a platinum (Pt) counter electrode, the sample as the working electrode, and a saturated calomel electrode (SCE) as the reference electrode. All the electrochemical measurements were performed at 25 °C in 5 mM H_2SO_4 solution. Before testing, the open circuit potential (OCP) was measured for 1 h in the test solution to ensure a stable state. The potentiodynamic polarization (PD) was performed with a scan rate of 0.167 mV s^{-1} in a potential window of -0.2 V$_{OCP}$ ~ 1.2 V$_{SCE}$. And the potentiostatic polarization (PS) was conducted with an applied voltage of 0.4 V$_{SCE}$ for 10 h. The Mott–Schottky analyses were performed with a scan rate of 40 mV s^{-1} and a fixed frequency of 1 kHz in a potential window of -0.8 V$_{SCE}$ ~ 0.8 V$_{SCE}$. The EIS experiment was recorded over a frequency range from 10^5 to 10^{-2} Hz with a potential perturbation of 10 mV and fitted by ZsimpWin software. Each test was repeated at least three times to ensure reproducibility.

Surface composition and morphology analysis

The phase composition of as-cast CoCrFeNiMo$_x$ HEAs was identified by X-ray diffractometer (XRD, Bruker D8 ADVANCE) within 2θ of 20° ~80° at a scanning rate of 2° min^{-1}. A scanning electron microscope (SEM, FEI Helios G4 CX) was applied to characterize the microstructure of the alloys. The electron backscatter diffraction (EBSD, FEI Helios G4 CX) patterns were acquired under the following conditions: an accelerating voltage of 20 kV, and a sample tilt of 70°. And the Volta potential maps were acquired by asscanning kelvin probe force microscopy (SKPFM, Bruker Dimension Icon). The chemical characteristics of the passive films formed at 0.4 V for 10 h were obtained using the X-ray photoelectron spectroscopy (XPS, PHI 5000 VersaProbe III) equipped with Al Kα Xray radiation operated at 50 W and 15 kV. The analysis area was set by an X-ray beam size of 200 μm in diameter. The surface was sputtered by Ar$^+$ ion bombardment every 6 s for 12cycles followed by 12 s for 11cycles with an ion beam of 2 keV and a 3×3 mm^2 area to obtain depth profiles. The analyzer pass energy was 280 eV for high-resolution spectra of Cr $2p_{3/2}$, Fe$2p_{3/2}$, Mo 3d, and O1s. All XPS peaks were calibrated to the standard carbon C1s peak (284.8 eV) and analyzed using the Multipak software.

REFERENCES

1. Cantor, B., Chang, I. T. H., Knight, P. & Vincent, A. J. B. Microstructural development in equiatomic multicomponent alloys. *Mat. Sci. Eng.: A.* **375**, 213–218 (2004).
2. Yeh, J. W. et al. Nanostructured high-entropy alloys with multiple principal elements: Novel alloy design concepts and outcomes. *Adv. Eng. Mater.* **6**, 299–303 (2004).
3. Manzoni, A. M. & Glatzel, U. New multiphase compositionally complex alloys driven by the high entropy alloy approach. *Mater. Charact.* **147**, 512–532 (2019).
4. Zhang, Y., Yang, X. & Liaw, P. K. Alloy design and properties optimization of high-entropy alloys. *Jom* **64**, 830–838 (2012).
5. Tian, Q. et al. The strengthening effects of relatively lightweight AlCoCrFeNi high entropy alloy. *Mater. Charact.* **151**, 302–309 (2019).
6. Gali, A. & George, E. P. Tensile properties of high- and medium-entropy alloys. *Intermetallics* **39**, 74–78 (2013).
7. Qiu, Y., Thomas, S., Gibson, M. A., Fraser, H. L. & Birbilis, N. Corrosion of high entropy alloys. *NPJ Mater. Degrad.* **1**, 15 (2017).
8. Ye, Q. et al. Microstructure and corrosion properties of CrMnFeCoNi high entropy alloy coating. *Appl. Surf. Sci.* **396**, 1420–1426 (2017).
9. Luo, H., Li, Z., Mingers, A. M. & Raabe, D. Corrosion behavior of an equiatomic CoCrFeMnNi high-entropy alloy compared with 304 stainless steel in sulfuric acid solution. *Corros. Sci.* **134**, 131–139 (2018).
10. Qiu, X. W., Zhang, Y. P. & Liu, C. G. Effect of Ti content on structure and properties of $Al_2CrFeNiCoCuTi_x$ high-entropy alloy coatings. *J. Alloy. Compd.* **585**, 282–286 (2014).
11. Wang, X. et al. Effect of Ti content on the microstructure and corrosion resistance of $CoCrFeNiTi_x$ high entropy alloys prepared by laser cladding. *Materials* **13**, 2209 (2020).
12. Kao, Y.-F., Lee, T.-D., Chen, S.-K. & Chang, Y.-S. Electrochemical passive properties of $Al_xCoCrFeNi$ (x = 0, 0.25, 0.50, 1.00) alloys in sulfuric acids. *Corros. Sci.* **52**, 1026–1034 (2010).
13. Lee, C. P., Chang, C. C., Chen, Y. Y., Yeh, J. W. & Shih, H. C. Effect of the aluminium content of $Al_xCrFe_{1.5}MnNi_{0.5}$ high-entropy alloys on the corrosion behaviour in aqueous environments. *Corros. Sci.* **50**, 2053–2060 (2008).
14. Shi, Y., Collins, L., Balke, N., Liaw, P. K. & Yang, B. In-situ electrochemical-AFM study of localized corrosion of $Al_xCoCrFeNi$ high-entropy alloys in chloride solution. *Appl. Surf. Sci.* **439**, 533–544 (2018).
15. Raza, A., Ryu, H. J. & Hong, S. H. Strength enhancement and density reduction by the addition of Al in CrFeMoV based high-entropy alloy fabricated through powder metallurgy. *Mater. Des.* **157**, 97–104 (2018).
16. Li, B.-y et al. Structure and properties of $FeCoNiCrCu_{0.5}Al_x$ high-entropy alloy. *T. Nonferr. Metal. Soc.* **23**, 735–741 (2013).
17. Clayton, C. R. & Lu, Y. C. A bipolar model of the passivity of stainless-steel-the role of Mo addition. *J. Electrochem. Soc.* **133**, 2465–2473 (1986).
18. Niu, Z., Wang, Y., Geng, C., Xu, J. & Wang, Y. Microstructural evolution, mechanical and corrosion behaviors of as-annealed $CoCrFeNiMo_x$ (x = 0, 0.2, 0.5, 0.8, 1) high entropy alloys. *J. Alloys Compd.* **820**, 153273 (2020).
19. Chou, Y. L., Yeh, J. W. & Shih, H. C. The effect of molybdenum on the corrosion behaviour of the high-entropy alloys $Co_{1.5}CrFeNi_{1.5}Ti_{0.5}Mo_x$ in aqueous environments. *Corros. Sci.* **52**, 2571–2581 (2010).
20. Liu, W. H. et al. Ductile $CoCrFeNiMo_x$ high entropy alloys strengthened by hard intermetallic phases. *Acta Mater.* **116**, 332–342 (2016).
21. Shun, T.-T., Chang, L.-Y. & Shiu, M.-H. Microstructure and mechanical properties of multiprincipal component $CoCrFeNiMo_x$ alloys. *Mater. Charact.* **70**, 63–67 (2012).
22. Guo, Y. et al. A superfine eutectic microstructure and the mechanical properties of $CoCrFeNiMo_x$ high-entropy alloys. *J. Mater. Res.* **33**, 3258–3265 (2018).
23. Shinomiya, H., Kato, Z. & Hashimoto, K. Spontaneous passivity of amorphous bulk Ni-Cr-Ta-Mo-Nb-P alloys in concentrated hydrochloric acids. *J. Solid State Electr.* **13**, 293–299 (2009).
24. Wang, Z., Zhang, L., Tang, X., Zhang, Z. & Lu, M. The surface characterization and passive behavior of Type 316L stainless steel in H_2S-containing conditions. *Appl. Surf. Sci.* **423**, 457–464 (2017).
25. Wang, Z., Feng, Z., Fan, X.-H. & Zhang, L. Pseudo-passivation mechanism of $CoCrFeNiMo_{0.01}$ high-entropy alloy in H_2S-containing acid solutions. *Corros. Sci.* **179**, 109146 (2021).
26. Dai, C., Zhao, T., Du, C., Liu, Z. & Zhang, D. Effect of molybdenum content on the microstructure and corrosion behavior of $FeCoCrNiMo_x$ high-entropy alloys. *J. Mater. Sci. Technol.* **46**, 64–73 (2020).
27. Bommersbach, P., Alemany-Dumont, C., Millet, J. P. & Normand, B. Formation and behaviour study of an environment-friendly corrosion inhibitor by electrochemical methods. *Electrochim. Acta* **51**, 1076–1084 (2005).
28. Fernandez-Domene, R. M., Blasco-Tamarit, E., Garcia-Garcia, D. M. & Garcia-Anton, J. Passive and transpassive behaviour of Alloy 31 in a heavy brine LiBr solution. *Electrochim. Acta* **95**, 1–11 (2013).
29. Ray, M. & Singh, V. B. Effect of sulfuric acid on corrosion and passivation of 316 SS in organic solution. *J. Electrochem. Soc.* **158**, C359–C368 (2011).
30. Della Rovere, C. A. et al. Characterization of passive films on shape memory stainless steels. *Corros. Sci.* **57**, 154–161 (2012).
31. Boissy, C., Ter-Ovanessian, B., Mary, N. & Normand, B. Correlation between predictive and descriptive models to characterize the passive film - Study of pure chromium by electrochemical impedance spectroscopy. *Electrochim. Acta* **174**, 430–437 (2015).
32. Cui, Z. et al. Influence of temperature on the electrochemical and passivation behavior of 2507 super duplex stainless steel in simulated desulfurized flue gas condensates. *Corros. Sci.* **118**, 31–48 (2017).
33. Chen, T. et al. Influence of surface modifications on pitting corrosion behavior of nickel-base alloy 718. Part 1: Effect of machine hammer peening. *Corros. Sci.* **77**, 230–245 (2013).
34. Inoue, A., Zhang, T. & Masumoto, T. Glass-forming ability of alloys. *J. Non-Cryst. Solids* **156**, 473–480 (1993).
35. Shuang, S., Ding, Z. Y., Chung, D., Shi, S. Q. & Yang, Y. Corrosion resistant nanostructured eutectic high entropy alloy. *Corros. Sci.* **164**, 108315 (2020).
36. Ningshen, S., Mudali, U. K., Mittal, V. K. & Khatak, H. S. Semiconducting and passive film properties of nitrogen-containing type 316LN stainless steels. *Corros. Sci.* **49**, 481–496 (2007).
37. Hakiki, N. E., Montemor, M. F., Ferreira, M. G. S. & Belo, M. D. Semiconducting properties of thermally grown oxide films on AISI 304 stainless steel. *Corros. Sci.* **42**, 687–702 (2000).
38. Pyun, S. I. & Kim, C. H. Determination of donor concentration in anodically passivation polycrystalline TiO_2 films from analysis of nonlinear mott-schottky plots. *Int. J. Hydrog. Energy* **16**, 661–664 (1991).
39. Jiang, R., Chen, C. & Zheng, S. The non-linear fitting method to analyze the measured M-S plots of bipolar passive films. *Electrochim. Acta* **55**, 2498–2504 (2010).
40. Sun, H., Wu, X. & Han, E.-H. Effects of temperature on the oxide film properties of 304 stainless steel in high temperature lithium borate buffer solution. *Corros. Sci.* **51**, 2840–2847 (2009).
41. Luo, H., Gao, S., Dong, C. & Li, X. Characterization of electrochemical and passive behaviour of Alloy 59 in acid solution. *Electrochim. Acta* **135**, 412–419 (2014).
42. Huang, J., Wu, X. & Han, E.-H. Electrochemical properties and growth mechanism of passive films on Alloy 690 in high-temperature alkaline environments. *Corros. Sci.* **52**, 3444–3452 (2010).
43. Yin, S. et al. Influence of specific second phases on corrosion behaviors of Mg-Zn-Gd-Zr alloys. *Corros. Sci.* **166**, 108419 (2020).
44. Lacroix, L., Ressier, L., Blanc, C. & Mankowski, G. Statistical study of the corrosion behavior of Al_2CuMg intermetallics in AA2024-T351 by SKPFM. *J. Electrochem. Soc.* **155**, C8–C15 (2008).
45. Oernek, C. & Engelberg, D. L. Correlative EBSD and SKPFM characterisation of microstructure development to assist determination of corrosion propensity in grade 2205 duplex stainless steel. *J. Mater. Sci.* **51**, 1931–1948 (2016).
46. Wang, L., Voyshnis, S., Seyeux, A. & Marcus, P. Ion transport mechanisms in the passive film formed on 304L stainless steel studied by ToF-SIMS with O-18 isotopic tracer. *Corros. Sci.* **173**, 108779 (2020).
47. Wang, L. et al. Electrochemical and XPS analytical investigation of the accelerative effect of bicarbonate/carbonate ions on AISI 304 in alkaline environment. *Appl. Surf. Sci.* **492**, 792–807 (2019).
48. Ye, W., Li, Y. & Wang, F. Effects of nanocrystallization on the corrosion behavior of 309 stainless steel. *Electrochim. Acta* **51**, 4426–4432 (2006).
49. Marcus, P. On some fundamental factors in the effect of alloying elements on passivation of alloys. *Corros. Sci.* **36**, 2155–2158 (1994).
50. Moravcik, I. et al. Interstitial nitrogen enhances corrosion resistance of an equiatomic CoCrNi medium-entropy alloy in sulfuric acid solution. *Mater. Charact.* **172**, 110869 (2021).
51. Shang, X.-L. et al. Effect of Mo addition on corrosion behavior of high-entropy alloys $CoCrFeNiMo_x$ in aqueous environments. *Acta Metall. Sin.-Engl.* **32**, 41–51 (2019).
52. Raza, A., Abdulahad, S., Kang, B., Ryu, H. J. & Hong, S. H. Corrosion resistance of weight reduced $Al_xCrFeMoV$ high entropy alloys. *Appl. Surf. Sci.* **485**, 368–374 (2019).
53. Ameer, M. A., Fekry, A. M. & Heakal, F. E. T. Electrochemical behaviour of passive films on molybdenum-containing austenitic stainless steels in aqueous solutions. *Electrochim. Acta* **50**, 43–49 (2004).
54. Dai, C. et al. X-ray photoelectron spectroscopy and electrochemical investigation of the passive behavior of high-entropy $FeCoCrNiMo_x$ alloys in sulfuric acid. *Appl. Surf. Sci.* **499**, 14390 (2020).

14

AUTHOR CONTRIBUTIONS
Q.H. and X.-Z.W. prepared the manuscript draft and performed material representation, Y.-P.Y. conducted all the electrochemical tests, S.-C.Z. helped with the results analyzes, C.-F.D. and H.W. helped modify the manuscript.

COMPETING INTERESTS
The authors declare no competing interests.

ADDITIONAL INFORMATION
Supplementary information The online version contains supplementary material available at https://doi.org/10.1038/s41529-022-00313-6.

Correspondence and requests for materials should be addressed to Xian-Zong Wang, Cheng-Feng Du or Haifeng Wang.

Reprints and permission information is available at http://www.nature.com/reprints